Journal of
Synchrotron Radiation

ISSN 0909-0495

Received 9 April 2012
Accepted 9 July 2012

Residual-density mapping and site-selective determination of anomalous scattering factors to examine the origin of the Fe *K* pre-edge peak of magnetite

Maki Okube,* Takuya Yasue and Satoshi Sasaki*

Materials and Structures Laboratory, Tokyo Institute of Technology, Nagatsuta 4259 (R3-11), Yokohama, Kanagawa 226-8503, Japan. E-mail: makisan@lipro.msl.titech.ac.jp, sasaki@n.cc.titech.ac.jp

The electron-density distribution and the contribution to anomalous scattering factors for Fe ions in magnetite have been analyzed by X-ray resonant scattering at the pre-edge of Fe *K* absorption. Synchrotron X-ray experiments were carried out using a conventional four-circle diffractometer in the right-handed circular polarization. Difference-Fourier synthesis was applied with a difference in structure factors measured on and off the pre-edge (E_{on} = 7.1082 keV, E_{off} = 7.1051 keV). Electron-density peaks due to X-ray resonant scattering were clearly observed for both *A* and *B* sites. The real part of the anomalous scattering factor f' has been determined site-independently, based on the crystal-structure refinements, to minimize the squared residuals at the Fe *K* pre-edge. The f' values obtained at E_{on} and E_{off} are −7.063 and −6.682 for the *A* site and −6.971 and −6.709 for the *B* site, which are significantly smaller than the values of −6.206 and −5.844, respectively, estimated from the Kramers–Kronig transform. The f' values at E_{on} are reasonably smaller than those at E_{off}. Our results using a symmetry-based consideration suggest that the origin of the pre-edge peak is Fe ions occupying both *A* and *B* sites, where *p*–*d* mixing is needed with hybridized electrons of Fe in both sites overlapping the neighbouring O atoms.

Keywords: X-ray resonant scattering; Fe_3O_4; magnetite; Fe *K* absorption edge; anomalous scattering factor; electron-density distribution.

1. Introduction

Taking account of the geometrical environment of 3*d* transition metals, the electron configuration changes drastically the *K*-edge spectra of X-ray absorption near-edge structure (XANES). In particular, the pre-edge peak is sensitive to the coordination number and the symmetry of a transition-metal polyhedron. Such pre-edge features as the peak energy and intensity distribution are also considered to change systematically with valence and spin states. For example, the intense pre-edge peak of X-ray absorption appears due to the electric dipole transition of tetrahedrally coordinated atoms such as Ti, V and Cr (Farges *et al.*, 1997; Tullius *et al.*, 1980; Pantelouris *et al.*, 2004). Although the electric dipole 1*s*–3*d* transition is forbidden by parity rules in a centrosymmetric site, weak pre-edge peaks have been reported for six-coordinated transition-metal compounds, *i.e.* Ti, V, Cr, Mn, Fe and Ni oxides (Farges *et al.*, 1997, 2001; Tanaka *et al.*, 1988; Pantelouris *et al.*, 2004; Farges, 2005; Westre *et al.*, 1997). In each case of transition-metal oxides, the electric quadrupole transition on 3*d* orbitals has been suggested, but much weaker than the dipole one. Both electric quadrupole and electric dipole transitions with 3*d*–4*p* mixing have been proposed to contribute to the pre-edge peak for the distorted octahedral site and tetrahedral site in Fe complexes (Westre *et al.*, 1997). Since the quadrupole transition is weak, the *p* mixing in the dipole transition becomes important in comparison with observed spectra and theoretical calculations. The importance of the *p* component in *d*–*p* hybridized orbitals has been reviewed on the pre-edge peak intensity for T_d and O_h symmetries (Yamamoto, 2008). A weak pre-edge peak of Fe *K* absorption was clearly observed in transition-metal ferrites of normal-spinel type, where Fe^{3+} occupies only octahedral sites (Matsumoto *et al.*, 2000). Therefore, it is expected in magnetite Fe_3O_4 that 4*p* mixing plays an important role in forming the pre-edge feature. Thus, we will focus our study on the occurrence of the pre-edge peak, using a new technique in combination with X-ray diffraction and absorption measurements at the Fe *K* edge.

Magnetite has an inverse-spinel-type crystal structure, as described in the chemical formula $[Fe^{3+}]^A[Fe^{2+}]^B[Fe^{3+}]^BO_4$.

Only Fe^{3+} ions occupy the tetrahedral *A* site, while Fe^{2+} and Fe^{3+} ions equally occupy the octahedral *B* site. Various physical properties of magnetite such as metallic behaviour, mixed valence and electron hopping are subject to the cation distribution between ferrous and ferric ions in the two kinds of site. The key to understanding these phenomena is 3*d* electrons. It is known in X-ray absorption experiments that magnetite has a pre-edge structure at the Fe *K* edge (Maruyama *et al.*, 1995). Since the electric dipole 1*s*–3*d* transition is generally prohibited for octahedral sites, the pre-edge peak of magnetite at the *K* absorption edge has been discussed to relate the Fe^{3+} ions at tetrahedral *A* sites, where the site symmetry of the sites is T_d ($\bar{4}3m$). Another possibility has also been proposed for magnetite in the electronic structure calculation by the local-spin density approximation (LSDA), where an *A*–O–*B* super-exchange interaction exists among the sites (Anisimov *et al.*, 1996).

The electric transition from 1*s* orbitals causes the X-ray resonant scattering (XRS) at the *K* absorption edge. Since the XRS reflects the electronic state well, it would be the best way to use the photon energy related to the specific electronic transition near the pre-edge. The XRS is defined by the anomalous scattering factor, and a site-independent determination is helpful in interpreting the origin of the pre-edge peak. The photon energy for the pre-edge study can be selected based on information from spectra of XANES as well as X-ray magnetic circular dichroism (XMCD). Most diffraction experiments to pinpoint photon energies with synchrotron radiation would require the anomalous scattering terms of the atomic scattering factor. The real part of the anomalous scattering factor f' can be suitably calculated based on relativistic wavefunctions and agrees considerably with experimental values at energies far from an absorption edge (Cromer & Liberman, 1970). Since the theoretical values are calculated for an isolated atom, they are not accurate enough in the energy region close to an absorption edge. There is a discrepancy due to a chemical shift by the oxidation state of the atom and the local chemical environment. Many attempts have been made near an absorption edge to measure anomalous scattering factors for relatively simple materials using various X-ray techniques, such as using an X-ray interferometer (Bonse & Materlik, 1976), the intensity ratio of Friedel-pair reflections (Fukamachi & Hosoya, 1975), total reflection measurement (Fukamachi *et al.*, 1978), the index of refraction through a prism (Fontaine *et al.*, 1985) and integrated intensity measurement (Templeton *et al.*, 1980). A realistic determination of f' may be to use the dispersion relation of the Kramers–Kronig integral because of its easy access to the data. Based on the X-ray absorption spectra measured with synchrotron radiation, f' values for GaAs, Ti, Ni and Cu were determined at the *K* edge from the imaginary part f'' (*e.g.* Fukamachi *et al.*, 1977; Hoyt *et al.*, 1984). However, once two or more crystallographic sites exist in the crystal structure, most of the above methods would be powerless for reasons of the requirement of a site-independent f'. In this study the integrated intensity method is adopted to observe the anomalous scattering effect for *A* and *B* sites in the magnetite structure. Similar approaches, site-specific studies on the diffraction anomalous fine structure and resonant magnetic Bragg scattering, have been reported for magnetite (Kobayashi *et al.*, 1998).

It is possible using X-ray diffraction techniques to pinpoint a specific atom by extracting resonantly scattered electrons. For example, the difference-Fourier synthesis emphasizing a difference in XRS intensity gives the residual electron density on a targeted atom. An analytical approach of using the shell structure factor has been proposed (Sasaki & Tsukimura, 1987). In the study of $(Co,Ni,Zn)SiO_3$, 1*s* core electrons are extracted from the total electrons to distinguish three kinds of transition-metal elements simultaneously occupying two crystallographic sites. Recently, the extraction analyses were extended to observe magnetic electron orbitals, by using the intensity difference in resonant X-ray magnetic scattering between left-handed and right-handed circular polarizations (Kaneko *et al.*, 2010). Applying the above technique to the electrons causing the pre-edge peak becomes important to confirm the origin of the pre-edge peak for magnetite.

In this study the origin of the pre-edge peak of magnetite will be discussed to determine the anomalous scattering factors and to make comparisons in residual electron-density maps between the *A* and *B* sites. The Fourier-synthesis technique, described as the electron-density difference $\Delta\rho(\mathbf{r}) = \rho(\mathbf{r})_{\rm on} - \rho(\mathbf{r})_{\rm off}$, is one such candidate in the use of the XRS intensity data measured at selective energies 'on' and 'off' the Fe *K* pre-edge peak.

2. Experimental

The magnetite used in this study was a highly stoichiometric sample which was grown from Fe_3O_4 powder in a Pt–10% Rh crucible by the Bridgman method in a CO–CO_2 atmosphere (Todo *et al.*, 2001). The cell dimension $a = 8.4000$ (3) Å and the space group is $Fd\bar{3}m$ (No. 227). A spherical single crystal of diameter 0.13 mm was mounted on a glass fiber for X-ray diffraction study.

The conventional measurements of integrated intensity were made using a Rigaku AFC7 four-circle diffractometer with a graphite (002) monochromator for Mo $K\alpha$ radiation ($\lambda = 0.71069$ Å). The intensity data were collected up to $\sin\theta/\lambda = 1.36$, in the range $-18 \le h_1,h_2,h_3 \le 18$ for reflection indices. The scan width and speed in ω were $1.5 + 0.3\tan\theta$ (°) and 1.0 (° $\rm min^{-1}$), respectively. The intensity variation of the three standard reflections was kept to less than ±1.5% throughout the data collection. Lorentz, polarization and spherical absorption effects were corrected for. The linear absorption coefficient was $\mu = 146.44$ $\rm cm^{-1}$. The transmission factors ranged from 0.289 to 0.333. In a total of 6228 reflections measured, 3016 reflections with $F > 3\sigma(F)$ were used for simultaneous refinements of a scale factor, an isotropic extinction parameter (Becker & Coppens, 1974), atomic coordinates and temperature factors. The function $\Sigma w_i(|F_{\rm obs}| - k|F_{\rm calc}|)^2$ was minimized, with $w_i = 1/\sigma^2(F)$ and k = a scale factor, by the full-matrix least-squares program *RADY* (Sasaki, 1987). Atomic scattering factors for Fe^{2+} and Fe^{3+}

(International Tables for X-ray Crystallography, 1974) and O^{2-} (Tokonami, 1965) were used in the refinements. Anomalous scattering factors were $f' = 0.301$ and $f'' = 0.845$. R and wR factors were 0.020 and 0.030, respectively.

All synchrotron experiments were performed at BL-6C and partly BL-10A of the Photon Factory, where a Si(111) double-crystal monochromator and (001) diamond phase retarder were used. The phase retarder produces circularly polarized X-rays, and was set near the 111 Bragg condition in the asymmetric Laue case and inclined by 45° from the vertical plane with σ and π components of the transmitted beam. For XMCD experiments, incident X-rays were alternately switched between right-handed and left-handed polarizations in each step of the monochromator. XMCD and XANES spectra were obtained from the same measurements in transmission mode. For diffraction experiments the right-handed circularly polarized X-rays were used with a Rigaku AFC5 four-circle diffractometer in the horizontal geometry of the scattering plane in order to prevent the intensity decreasing with linear polarization. The energy calibration was carefully carried out in the XANES spectrum using an inflection point (E = 7.1120 keV, λ = 1.7433 Å) of Fe metal foil of thickness 5 µm (Bearden & Burr, 1989; Sasaki, 1995). The X-ray energy in keV was converted to wavelength in Å using a factor of 12.398 (Thompson *et al.*, 2001).

The absorption measurements were made using a beam size of 1 mm × 2 mm at the Fe K edge with two ionization chambers filled with N_2 (monitor) and 85% N_2 + 15% Ar gas. The external magnetic field was 0.4 T *via* a pair of rare-earth magnets in the Faraday configuration. The thickness of the samples was adjusted for the suitable absorption. The incident and absorbed intensities were measured at a measuring time of 80 s with variable step-widths from 0.2 to 11 eV of the monochromator (Okube *et al.*, 2002). Powder samples of magnetite were used as-received (Kojundo Chemical Laboratory, 99%). Powder samples of Ni ferrite ($NiFe_2O_4$) were used as a typical sample having pure Fe^{3+} spectra for XANES measurements. Ni ferrite was grown from stoichiometric mixtures of NiO and Fe_2O_3 at a temperature of T = 1273 K for two days, after pre-heating in evacuated silica tubes at 1000 K for two days.

Diffraction intensity measurements on synchrotron X-rays were carried out in the top-up operation mode with the AFC5 diffractometer at photon energies of E_{on} = 7.1082 keV (λ = 1.7442 Å) and E_{off} = 7.1051 keV (λ = 1.7449 Å). The linear absorption coefficients were 334.53 and 224.97 cm^{-1}, which are relatively small because of the pre-edge region. The transmission factors for the E_{on} and E_{off} data sets ranged from 0.061 to 0.108 and from 0.131 to 0.177, respectively. Bragg peaks were repeatedly scanned having a width of 1.0° in ω and a scan speed of 0.5° min^{-1}. In total, 354 reflections up to $\sin\theta/\lambda$ = 0.4 were measured in the range $-6 \le h_1,h_2,h_3 \le 6$. The integrated intensity of a standard reflection was collected every 50 measurements and used for the correction. Lorentz and polarization effects and spherical absorption effects were corrected for before crystal-structure analyses. The reflections having $F \ge 3\sigma(F)$ were averaged among all symmetrical-equivalent reflections and used in this study. Crystal-structure analyses with isotropic extinction correction (Becker & Coppens, 1974) were carried out using *RADY*. Anomalous scattering factors were used after the estimation in this study. In the refinement procedure, atomic coordinates and anisotropic temperature factors were first refined using the Mo $K\alpha$ data set. Final R and wR factors for the 'on' refinements were 0.048 and 0.057, while the factors for 'off' are 0.050 and 0.061, respectively.

3. Wavelength selection and Kramers–Kronig transforms

XMCD reflects the spin and orbital polarization of the unoccupied states of an atom. In this study, unpaired 3d–4p electronic orbitals were targeted. According to the Lambert–Beer equation, $I = I_0\exp(-\mu t)$, the spin-dependent part of absorption can be defined as

$$\Delta\mu t = \mu^+ t - \mu^- t = \ln\left(I_0^+/I^+\right) - \ln(I_0^-/I^-), \qquad (1)$$

where μ and $\Delta\mu$ are the total and spin-dependent absorption coefficients with sample thickness t. I_0 and I are the incident and absorbed X-ray intensities, having symbols + and − for parallel and antiparallel measurements between photon and spin directions, respectively. The thickness-free normalization is then given by $\Delta\mu/\mu$, with the XANES absorption intensity calculated from the coefficients μ^+ and μ^-. The XMCD and XANES spectra are shown in Fig. 1. It is known that the XANES threshold spectra of magnetite parallel the Fe^{2+} spectra of FeO and Fe^{3+} spectra of Fe_2O_3. The chemical shift between ferrous and ferric ions is about 5 eV, where experi-

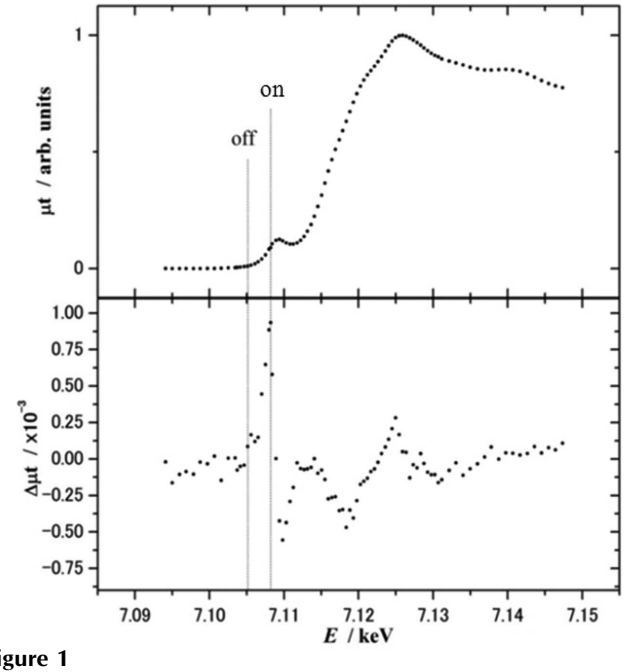

Figure 1
XANES (top) and XMCD (bottom) spectra of magnetite. The photon energy marked 'on' gives the position of a positive XMCD peak (E_{on} = 7.1082 keV), while the energy at 'off' stands apart from the pre-edge peak (E_{off} = 7.1051 keV).

mental f' values of Fe^{2+} and Fe^{3+} were previously estimated from the absorption curves at the Fe K edge (Sasaki, 1995; Okube *et al.*, 2008). By the valence-difference contrast method applied for magnetite, the valence fluctuation and charge ordering were detected in X-ray observations of diffuse scattering and superlattice reflections, respectively (Toyoda *et al.*, 1997, 1999).

The photon energy marked 'on' in Fig. 1 is E_{on} = 7.1082 keV, which corresponds to an XANES peak at the Fe K pre-edge and a positive peak of the dispersive XMCD signal. The energy E_{off} (= 7.1051 keV) was selected for comparison with the pre-edge effect. The 'off' position stands apart from the pre-edge towards the lower-energy side.

The crystal structure factor $F(hkl)$ at an hkl reciprocal lattice point can be written as

$$F(hkl) = \sum_j f_j \exp 2\pi i(hx_j + ky_j + lz_j) \exp(-W_j), \qquad (2)$$

for the jth atom with fractional coordinates x_j, y_j and z_j and Debye–Waller factor W_j. Then, the atomic scattering factor f is given by

$$f = f_0(\sin\theta/\lambda) + f'(E) + if''(E), \qquad (3)$$

for photon energy E. The Thomson elastic scattering f_0 depends on the scattering angle 2θ. The anomalous scattering effect is dominant near the absorption edge, where the real part $f'(E)$ gives strong contrast in X-ray diffraction. The imaginary term $f''(E)$ is determined from the absorption effect. $f'(E)$ can be generally calculated from $f''(E)$ by the Kramers–Kronig dispersion relation, written as

$$f'(\omega_0) = (2/\pi) \int_0^\infty \omega f'(\omega)/(\omega_0^2 - \omega^2)\, d\omega \qquad (4)$$

for angular frequency ω of the incident X-rays. The program *DIFFKK* (Cross *et al.*, 1998) was used in our calculations with the absorption data, avoiding the singularity at the point $\omega = \omega_0$ in (4) and matching the theoretical approach by, for example, Cromer & Liberman (1970). The observed values of the imaginary part $f''(E)$ were obtained from the absorption coefficients derived from the XANES spectra of $NiFe_2O_4$ ferrite near the Fe K edge, which are shown in the upper part of Fig. 3. The cross sections of the theoretical absorption were extended to the unobserved energy region by the *ab initio* Cromer & Liberman calculation, based on an isolated-atom model. The integration on the real part $f'(E)$ was separated into blocks of conjugate pairs for the calculation far from the edge.

In order to simplify the comparable model, the XANES spectra of $NiFe_2O_4$ were used as the absorption data to estimate $f'(E)$. $NiFe_2O_4$ has the same inverse-spinel structure, containing only Fe^{3+}. The XANES and XMCD spectra of Ni ferrite are compared with those of magnetite in Fig. 2. It is reported in a solid solution of $(Ni^{2+}, Fe^{2+})Fe^{3+}{}_2O_4$ that the absorption spectra between Fe_3O_4 and $NiFe_2O_4$ resemble each other especially in the pre-edge region (Saito *et al.*, 1999). By transforming from the imaginary term $f''(E)$ to normalize XANES spectra, an energy-dependent curve of $f'(E)$ was

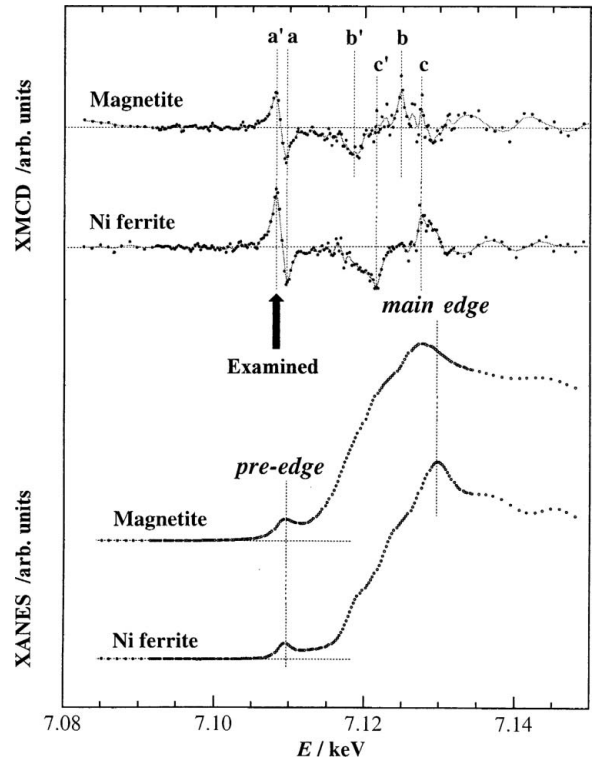

Figure 2
XANES (bottom) and XMCD (top) spectra of magnetite and Ni ferrite. Both crystals have the inverse-spinel structure. Ni ferrite includes only Fe^{3+}, while magnetite is a mixture of Fe^{2+} and Fe^{3+}. The peaks of XANES and XMCD spectra are very close to each other in the vicinity of the Fe K pre-edge. Photon energies of XMCD peaks at E = 7.108, 7.110, 7.119, 7.125, 7.122 and 7.129 keV are donoted a', a, b', b, c' and c, respectively.

obtained in the Kramers–Kronig dispersion relation, shown in the lower half of Fig. 3. The real and imaginary parts of the anomalous scattering factor of Fe^{3+} were thus derived to be $f' = -6.206$ and $f'' = 0.420$ at E_{on} and $f' = -5.844$ and $f'' = 0.374$ at E_{off}, respectively.

4. Determination of f' by crystal-structure analyses

The crystal structure of magnetite has been studied by various authors (Nishikawa, 1915; Bragg, 1915*a*,*b*; Claassen, 1926; Verwey & Boer, 1936; Verwey *et al.*, 1947; Fleet, 1981; Okudera *et al.*, 1996; Sasaki, 1997). A general view of the structure is illustrated in Fig. 4. Oxygen atoms are approximately located in cubic closest packing and their coordinates are called the u-parameter. Fe atoms in the octahedral B site have diagonal chains along the ⟨110⟩ directions, linked by Fe atoms in tetrahedral A sites obliquely above and below the B chains (Fig. 4*b*). The B chains alternately lie in [100] and [$\bar{1}$10]. This is interpreted such that valence fluctuation and electron hopping cause a continuous interchange of electrons between Fe^{2+} and Fe^{3+} diagonally among the Fe ions forming the B-site chains in the ⟨110⟩ directions. Structural parameters were also refined in this study by using the Mo $K\alpha$ data set. Atomic coordinates x_1 (= x_2 = x_3) of tetrahedral A (8*a*), octahedral B (16*d*) and oxygen 32*e* sites are 1/8, 1/2 and 0.25494 (6), respectively, in the setting for the origin at the centre of

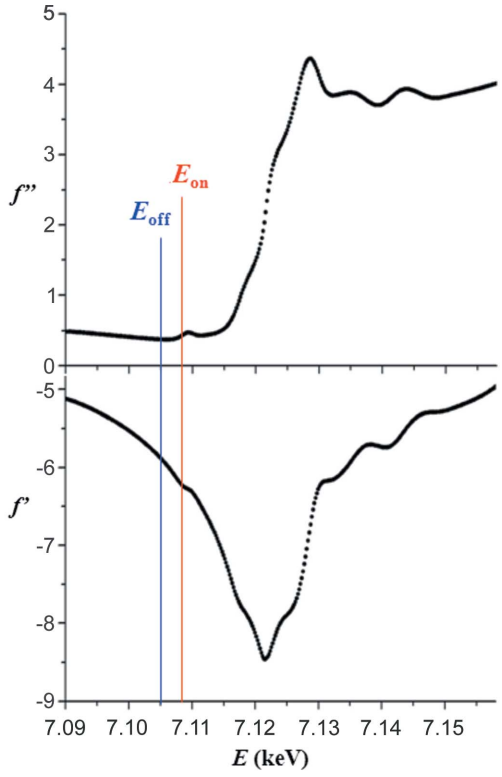

Figure 3
Curves of $f'(E)$ (bottom) and $f''(E)$ (top) for Fe^{3+} of Ni ferrite related to the Kramers–Kronig transform. The vertical lines indicate photon energies E_{on} and E_{off} which were used for X-ray diffraction experiments.

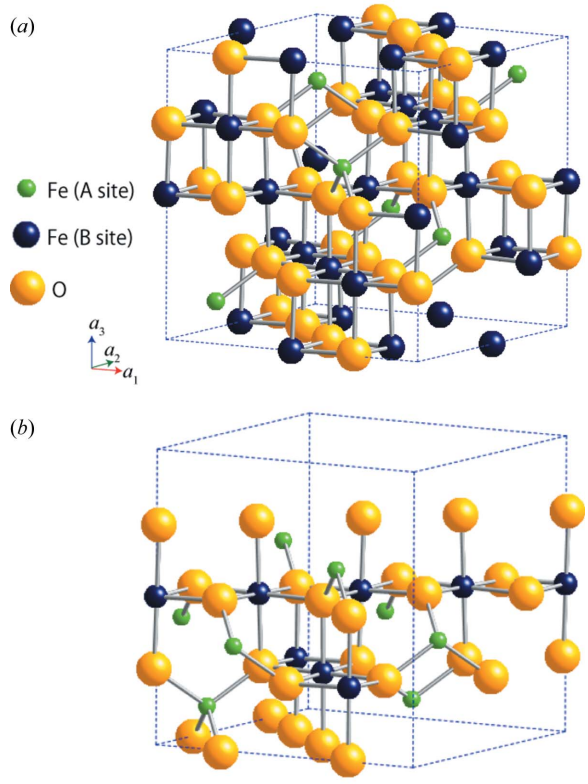

Figure 4
Crystal structure of magnetite in the origin at centre ($\bar{3}m$). (*a*) Overview of the crystal structure and (*b*) schematic drawing of the linkage and bonding around the *A* and *B* sites.

symmetry. The bond distances and angle of Fe(*A*)—O, Fe(*B*)—O and ∠[Fe(*A*)—O—Fe(*B*)] are 1.8906 (3) Å, 2.0594 (5) Å and 123.63 (2)°, respectively. The thermal parameters are: β_{11} = 0.001408 (4) and β_{12} = 0 for the *A* site; β_{11} = 0.001893 (3) and β_{12} = 0.000184 (4) for the *B* site; β_{11} = 0.001861 (7) and β_{12} = −0.00012 (1) for the oxygen site, where the constraints are $\beta_{11} = \beta_{22} = \beta_{33}$ and $\beta_{12} = \beta_{13} = \beta_{23}$.

Having a high photon energy, sufficient to promote an electric transition in an atom, the resonant scattering becomes dominant close to the absorption edge and the real term of the anomalous scattering factor $f'(E)$ in (3) has a deep minimum at the Fe *K* edge. As shown in Fig. 3, the pre-edge structure appears in the $f'(E)$ curve after the Kramers–Kronig dispersion transform. Although a spectroscopic study of absorption does not detail the site-separated information between the *A* and *B* sites, the diffraction technique is of advantage in distinguishing the scattering from the two sites. The f' term in the atomic scattering factor f was determined site-independently for independent j described in (2). Then, the multiplicity parameter of f' was refined with a scale factor in the least-squares calculation to minimize the sum of squared residuals in the function $\Sigma w_i(|F_{obs}| - |F_{calc}|)_i^2$. The best-fitting curves for the *A* and *B* sites were obtained from the intensity data measured at E_{on} and E_{off} (Fig. 5). The variation of residual factors has a minimum against parameter f', indicating good convergence. The f' values obtained for the Fe ions are summarized in Table 1, and are −7.063 and −6.971 at E_{on} and −6.682 and −6.709 at E_{off} for the *A* and *B* sites, respectively. These values are almost identical between the two sites but the *A* site has more negative values. The differences $f'_{on} - f'_{off}$ are reasonably negative, −0.381 and −0.262 for Fe in the *A* and *B* sites, respectively. Two types of anomalous scattering factors were obtained by the following approaches: (i) structure-factor analysis of magnetite and (ii) Kramers–Kronig transform of $NiFe_2O_4$. The difference in f' between the two approaches are −0.811 and −0.812 at E_{on} and E_{off}, respectively. It should be noted that the f' values of magnetite are smaller than those of $NiFe_2O_4$, owing to the presence of one extra electron of Fe^{2+} in magnetite.

5. Electron-density distributions on pre-edge resonance

The partitioning of f' in reciprocal space is helpful to visualize part of the electron densities resonating at the pre-edge, which are Fourier synthesized from X-ray diffraction data of magnetite. The difference between observed and calculated structure factors appears on the difference-Fourier map to calculate the Fourier coefficients $[|F_{obs}(hkl)| - |F_{calc}(hkl)|]$. Since the calculated model generally does not yield the whole scattering power of all the atoms in the structure solution, the difference-Fourier method is widely used to complete the structural model by supplying the difference in electron density between $\rho_{obs}(\mathbf{r})$ and $\rho_{calc}(\mathbf{r})$. When the X-ray resonant scattering effect is applied to squeeze part of the electrons

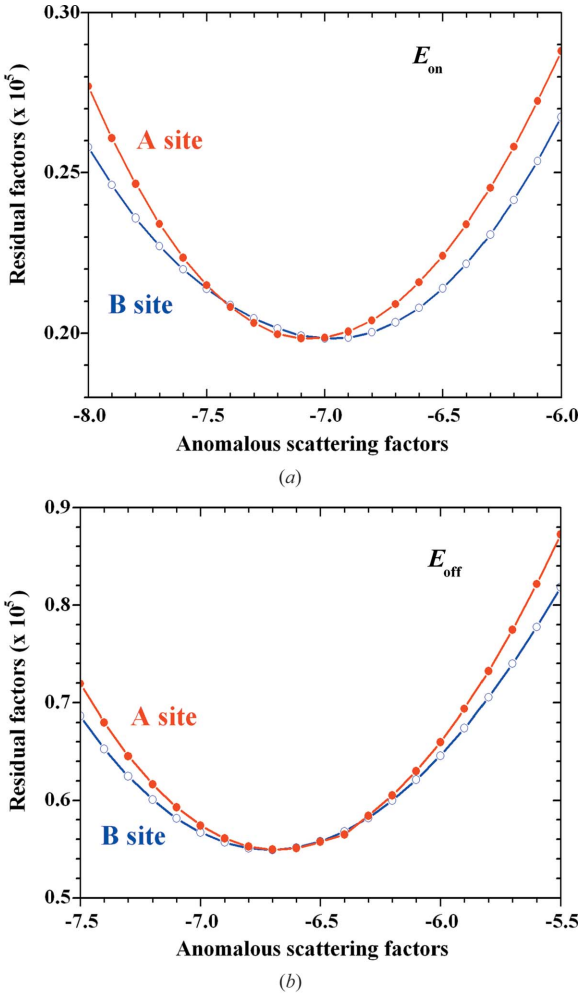

Figure 5
Variation of the residual factors $\Sigma w_i(|F_{obs}| - |F_{calc}|)_i^2$ as a function of the real part of the anomalous scattering factors f'. The least-squares calculations were made site-independently for the A and B sites, using the intensity data at (*a*) E_{on} and (*b*) E_{off} around the Fe K pre-edge.

between the energy E_{on} and E_{off} at the Fe K pre-edge, the difference in electron density $\Delta\rho(\mathbf{r})$ is given by

$$\Delta\rho(\mathbf{r}) = V^{-1}\sum\sum\sum |F_{obs}(hkl, E_{on})| - |F_{obs}(hkl, E_{off})| \times \exp 2\pi i\varphi_{calc}(hkl)\exp(-2\pi i\mathbf{k}\cdot\mathbf{r}), \quad (5)$$

where $\varphi_{calc}(hkl)$ is the phase term and $\mathbf{r}$, V and $\mathbf{k}$ are the positional vector, unit cell volume and scattering vector, respectively. The summation in crystallographic Fourier series is always finite, because only a finite number of Bragg reflections is observable for the estimation. Since the observation is assumed to be identical to the calculation beyond an upper limit on the summation, the difference-Fourier synthesis has merit in the removal of the termination effect of the Fourier series by subtraction. The main contribution in (5) comes from the difference between $f'(E_{on})$ and $f'(E_{off})$ in (3). After removal of the calculated model defined as an observation at E_{off}, the residual density constitutes the valence electrons, where 3*d*–4*p* electrons are assumed to partly cause the electronic transition at the Fe K pre-edge. Since the crystallographic errors are considered to be cancelled out, some $F_{obs}(hkl)$ can be replaced by $F_{calc}(hkl)$. Then (5) is rewritten as

$$\Delta\rho(\mathbf{r}) \simeq V^{-1}\sum\sum\sum \Big(\Big\{\big[|F_{obs}(hkl, E_{on})| - |F_{obs}(hkl, E_{off})|\big] / |\langle F_{obs}(hkl)\rangle| + 1\Big\}|\langle F_{calc}(hkl)\rangle| - |F_{calc}(hkl, E_{off})|\Big) \times \exp(-2\pi i\mathbf{k}\cdot\mathbf{r}). \quad (6)$$

Based on (6), difference-Fourier syntheses were carried out to emphasize the effect of $f'(E_{on}) - f'(E_{off})$ using the software *FRAXY*. Fig. 6 shows typical two-dimensional maps of planes passing through x_1 = 1/8 and x_1 = 1/2 in magnetite, where triclinic structure factors were used without any symmetrical restriction. Fe ions in the A and B sites of magnetite are located at the centres of the maps in Figs. 6(*a*) and 6(*b*), respectively. Positive and zero-level density contours are shown by solid lines, while dotted lines indicate negative levels of electron density.

Negative peaks for Fe atoms were observed at the centres of both the A and B sites of magnetite on the $(0h_2h_3)$ planes in Fig. 6, where contours are drawn at 0.5 e Å^{-3} intervals. The density heights are −2.7 and −2.9 e Å^{-3} for the A and B sites, respectively. It is noted that the maps contain spurious positive peaks which may appear due to the scaling effect to fit $F_{obs}(hkl)$ to $F_{calc}(hkl)$ in the least-squares refinements. The appearance of the negative peaks can be explained well by our results that the $f'(E_{on})$ value is always smaller than the $f'(E_{off})$ value. Generally, the electron density of the Fe atom is estimated to be 215.6 e Å^{-3} for an isotropic temperature factor B = 1.0 (Sakurai, 1967). Therefore, the peak heights, to be around $\Delta\rho$ = −3 e Å^{-3} so far examined in this study, are within a reasonable order in rough comparison between f (∼20) and $f'(E_{on} - E_{off})$ (∼0.3). Our analysis makes only the electrons related to the Fe K pre-edge peak visible at some specific energy level E_{on}, suggesting the existence of electrons resonantly scattered for both A and B sites.

Table 1
Experimental f' values and some f'' differences for Fe ions near the Fe K pre-edge.

	'On'	'Off'	$f'_{on} - f'_{off}$
E (keV)	7.1082	7.1051	
λ (Å)	1.7442	1.7449	
f' (bulk†, K–K transform)	−6.206	−5.884	−0.322
f''	0.420	0.374	
f' (A site, structure analysis)	−7.063	−6.682	−0.381
f' (B site, structure analysis)	−6.971	−6.709	−0.262
f' (average of two sites)	−7.017	−6.696	−0.321
Site difference ($A - B$)	−0.092	−0.027	−0.239

† Fe^{3+} in $NiFe_2O_4$ ferrite (inverse-spinel structure).

6. Peak origin and density of states

At the first stage of the X-ray absorption experiments of ferrite the pre-edge peak was considered to originate from the atoms occupying the tetrahedral A site. From a cluster-model calculation, the dispersion-type XMCD was also explained as the 1*s* to 3*d* dipole transition allowed at the A site, having

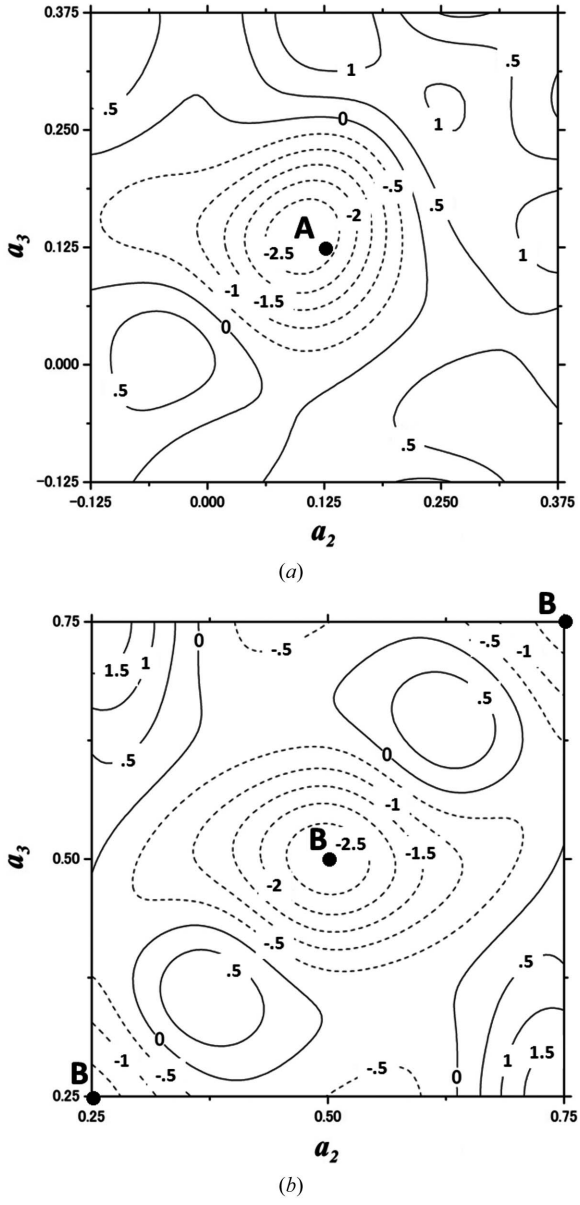

Figure 6
Partial electron-density maps for (*a*) *A* and (*b*) *B* sites of magnetite on $(0h_2h_3)$ in e Å^{-3}. The maps corresponding to the partitioning of $f'(E)$ were synthesized with the Fourier coefficients of $[|F_{obs}(E_{on})| - |F_{obs}(E_{off})|]$. In the figures, the *A* and *B* sites are located at the positions (1/8,1/8,1/8) and (1/2,1/2,1/2), respectively, and pass through (*a*) $x_1 = 1/8$ and (*b*) $x_1 = 1/2$. Contours are at intervals of 0.5 e Å^{-3}. Solid lines indicate positive density including zero, and broken lines indicate negative ones.

hybridization between the Fe 3*d*–4*p* and O 2*p* orbitals (Maruyama *et al.*, 1995). On the other hand, ATS (anisotropic tensor of susceptibility) studies found the pre-edge of magnetite which strongly suggested contribution from the *B* site, because the dipole transition of Fe in the *A* site cannot excite the ATS scattering (Hagiwara *et al.*, 1999; Kanazawa *et al.*, 2002; Subias *et al.*, 2004, 2009). In our study negative peaks were observed both in the *A* and *B* sites (Fig. 6), which are a result of the difference in XRS between E_{on} and E_{off}. This observation is consistent with those of various works on high-spin ferric complexes having O_h and T_d symmetries. The pre-edge feature is sensitive to the coordination number and symmetry, as well as valence and spin states. The intensity of the pre-edge peak for high-spin ferric complexes with O_h symmetry is weak but sufficiently observed. When *p* mixing does not exist, the only mechanism producing the intensity in the O_h field is the electric quadrupole transition in the 1*s* to 3*d* transition. There is a clear split feature in the Fe *K*-edge spectra of FeF_3, $FeCl_3$, $FeBr_3$, $[FeCl_6][Co(NH_3)_6]$ and $Fe(acac)_3$, where acac is acetylacetonate (Westre *et al.*, 1997). Since the ground state of the high-spin Fe^{3+} has a $(t_{2g})^3(e_g)^2$ spin configuration, there are two spin configurations of $(t_{2g})^2(e_g)^2$ and $(t_{2g})^3(e_g)^1$ available for the excited state. The configuration suggests the possibility that Fe in the octahedral site gives two peaks at the pre-edge. There is an example of $Fe(acac)_3$ having two pre-edge peaks with splitting at about 1.5 eV and an intensity ratio of 3:2 (Westre *et al.*, 1997). On the other hand, in the case of high-spin ferric complexes with T_d symmetry, a more intense peak is generally observed at the pre-edge because the dipole mechanism of 3*d* orbitals is associated with 4*p* mixing. The ground state of the high-spin Fe^{3+} has an $(e)^2(t_2)^3$ configuration, while the excited state from 1*s* to 3*d* gives two spin configurations of $(e)^1(t_2)^3$ and $(e)^2(t_2)^2$ with very small peak-splitting.

For high-spin ferrous complexes, the pre-edge peak has also been observed with O_h symmetry. Wu *et al.* (2004) have assigned the first pre-edge peak of Fe^{2+} in NaCl-structure-type FeO at the energy to a direct quadrupole transition, by comparing the multiple-scattering calculation with experimental spectra at the Fe *K* edge. Similar to the other divalent transition-metal oxides such as MnO and CoO, the pre-edge structure of Fe_2SiO_4 was observed by fluorescence-detected XANES and is well reproduced with three peaks from crystal-field multiplet calculations (Groot *et al.*, 2009). Since magnetite has a mixed valence state between Fe^{2+} and Fe^{3+} at room temperature, Fe 3*d* in the *B* site has one extra electron to fill the t_{2g} orbitals, compared with high-spin ferric complexes. Although a difference in f' between Fe^{2+}–Fe^{3+} mixing and pure Fe^{3+} was observed in this study, only the high-spin Fe^{3+} case is included in the electronic structure of magnetite because the discussion requires further theoretical treatment for electron hopping.

The electronic structure of magnetite has been calculated for the local-spin density approximation (LSDA) with density-function theory (Yanase & Siratori, 1984; Zhang & Satpathy, 1991; Anisimov *et al.*, 1996). The ferrimagnetic model gives a magnetic moment of 4 μ_B per formula unit in the half-metallic state. The magnetic moment for the model having antiparallel moment is in agreement with the observed value of 4.1 μ_B, according to saturation magnetization measurements (Gorter, 1954; Groenou *et al.*, 1968); namely, since the high-temperature phase of magnetite, having the inverse-spinel structure, is ferrimagnetic with a Neel temperature of 793 K. The magnetic moments of Fe^{2+} and half of Fe^{3+} in the *B* sites are regarded to align antiparallel to those of Fe^{3+} in the *A* sites. Fig. 7 shows a schematic diagram of the excited state from 1*s* to 3*d* for Fe of magnetite. The density of states in the LSDA calculation (Anisimov *et al.*, 1996) is used with the vertical energy axis,

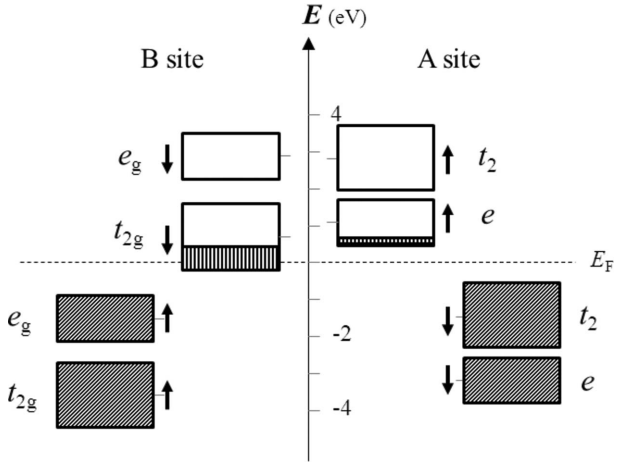

Figure 7
Schematic diagram of the density of states for Fe^{3+} in the *B* and *A* sites of Fe_3O_4. The diagram was drawn based on the LSDA calculation reported by Anisimov *et al.* (1996).

where the Fermi energy lies in the t_{2g} band of the *B* site. Below the Fermi level, up-spin t_{2g} and e_g bands and down-spin *e* and t_2 bands of Fe sequentially exist above the oxygen band between −8 and −4 eV in the *B* and *A* sites, respectively. Reversely, up-spin *e* and t_2 bands and down-spin t_{2g} and e_g bands of Fe exist above the Fermi level in the *A* and *B* sites, respectively. The photon energy in our experiment was selected at the position of a positive XMCD peak, indicated as 'on' in Fig. 1 and *a*′ in Fig. 2. According to the schematic diagram just above the Fermi energy shown in Fig. 7, the photon energy corresponds to the lower part of the t_{2g} orbitals in the *B* site and partly the lowest region of the *e* orbitals in the *A* site. The orbitals are drawn as vertical stripes in Fig. 7. Although the energy region indicating the *A* site is shallow near the plains at the foot of the transition-intensity peak, the excited state sufficiently affects the observation of the pre-edge peak because of high transition probability.

Again, in 3*d* electrons in the FeO_6 octahedron, the appearance of the pre-edge peak is prohibited by the selection rule within the dipole transition in the regular octahedron and requires another contribution from the quadrupole transition or from the hybridization controlled by the symmetry with neighbouring ions. It should be mentioned here that the point group of the *B* sites of magnetite is not O_h ($4/m\ \bar{3}\ 2/m$) but D_{3d} ($\bar{3}\ 2/m\ 1$). The electronic dipole mechanism from 1*s* to 3*d* orbitals involves mixing of 4*p* character in the non-centrosymmetric Fe site. Including the second-neighbour or farther atoms around the *B* site, the dipole transition in the (. $\bar{3}\ 2/m$) site symmetry is allowable to form *p*–*d* hybridized orbitals to be trigonalized. On the other hand, in the *A* site having $\bar{4}3m$ site symmetry, electric dipole transitions from a 1*s* electron are possible with *p*–*d* hybridized orbitals and quadrupole transition. Thus, it would be conclusive that the dipole and quadrupole transitions for Fe ions in both *A* and *B* sites are allowable at the pre-edge.

Ferrimagnetic ordering takes place in competition with super-exchange interactions between Fe ions in the *A* and *B* sites mediated by O atoms. The super-exchange interactions for straight *A*—O—*B* bonding occur through combination of a σ-bond through the e_g orbitals and a π-bond through the t_{2g} orbitals. In other cases having kinked *A*—O—*B* bonds, the exchange integrals of J_{AB} (*A*—O—*B*), J_{AA} (*A*—O—*A*) and J_{BB} (*B*—O—*B*) characterize the super-exchange interactions. First-principle studies of exchange integrals for magnetite can reproduce the Curie temperature, having exchange constant values of J_{AA} = −0.18 meV, J_{BB} = 0.83 meV and J_{AB} = −2.88 meV in the nearest-neighbour approximation (Uhl & Siberchicot, 1995). The ferrimagnetic arrangement of magnetic moments suggests that J_{AB} is stronger than the others in magnetite because of the geometry of the 3*d* orbitals involved, consistent with the *A*—O—*B* bond angle of 123.63 (2)°. Thus, since the hybridization with the *A*—O—*B* super-exchange interaction is common in the ferrite structure, it is natural that the Fe 3*d*–4*p* orbital is connected with the neighbouring Fe through O 2*p*. Although the O 2*p* orbitals take an important role to stabilize the high-spin state of Fe^{3+} in magnetite, the contribution to the electronic structure needs more accurate theoretical calculations in the geometrically frustrated system. In the theoretical LSDA calculation partly shown in Fig. 7, the O 2*p* orbitals are located about 7 eV lower than the Fermi level (Anisimov *et al.*, 1996). The energy may be much higher from a view of our empirical knowledge. The *A*—O—*B* ferrimagnetic scheme has been sufficiently obtained to have empty bands of up-spin *A* and down-spin *B* sites just above the Fermi level. The nature of the pre-edge peak must help the interpretation of the electronic structure of Fe ions with their neighbours and the physical properties of transition-metal oxides.

7. Conclusion

Anomalous scattering factors determined by the crystal-structure analysis for Fe ions of the *A* and *B* sites are −7.063 and −6.971 at E_{on} (= 7.1082 keV) of the Fe *K* pre-edge and −6.682 and −6.709 at E_{off} (= 7.1051 keV) off the edge. From the difference-Fourier syntheses to extract the intensity difference between E_{on} and E_{off}, negative electron densities related to the X-ray resonant scattering were clearly observed in the peak tops of Fe ions in both *A* and *B* sites. The above results have led to our conclusion that Fe ions occupying *A* and *B* sites contribute to the Fe *K* pre-edge peak of magnetite.

The authors are grateful to Professors S. Todo and H. Kawata for providing a single crystal of magnetite. We are thankful to Mr Naoto Shibuichi for our *DIFFKK* calculations. We also thank Professor H. Kawata and Mr H. Ohta for their support at BL-6C. This study was performed under the auspices of the Photon Factory (PAC No.2009G104, 2010G524 and 2011G517). This work was supported in part by Grant-in-Aids (No. 24360007 and No. 24740354).

References

Anisimov, V. I., Elfimov, I. S., Hamada, N. & Terakura, K. (1996). *Phys. Rev.* **54**, 4387–4390.
Bearden, J. A. & Burr, A. F. (1989). *Rev. Mod. Phys.* **39**, 125–142.

Becker, P. J. & Coppens, P. (1974). *Acta Cryst.* A**30**, 129–147.
Bonse, U. & Materlik, G. (1976). *Z. Phys. B*, **24**, 189–191.
Bragg, W. H. (1915*a*). *Nature (London)*, **95**, 561.
Bragg, W. H. (1915*b*). *Philos. Mag.* **30**, 305–315.
Claassen, A. A. (1926). *Proc. Phys. Soc. London*, **38**, 482–487.
Cromer, D. T. & Liberman, D. A. (1970). *J. Chem. Phys.* **53**, 1891–1898.
Cross, J. O., Newville, M., Rehr, J. J., Sorensen, L. B., Bouldin, C. E., Watson, G., Gouder, T., Lander, G. H. & Bell, M. I. (1998). *Phys. Rev. B*, **58**, 11215–11225.
Farges, F. (2005). *Phys. Rev. B*, **71**, 155109.
Farges, F., Brown, G. E., Petit, P.-E. & Munoz, M. (2001). *Geochim. Cosmochim. Acta*, **65**, 1665–1678.
Farges, F., Brown, G. E. & Rehr, J. J. (1997). *Phys. Rev.* B**56**, 1809–1819.
Fleet, M. E. (1981). *Acta Cryst.* B**37**, 917–920.
Fontaine, A., Warburton, W. K. & Ludwig, K. F. (1985). *Phys. Rev. B*, **31**, 3599–3605.
Fukamachi, T. & Hosoya, S. (1975). *Acta Cryst.* A**31**, 215–220.
Fukamachi, T., Hosoya, S., Kawamura, T., Hunter, S. & Nakano, Y. (1978). *Jpn. J. Appl. Phys.* **17**, 326–328.
Fukamachi, T., Hosoya, S., Kawamura, T. & Okonuki, M. (1977). *Acta Cryst.* A**33**, 54–58.
Gorter, E. W. (1954). *Philips Res. Rep.* **9**, 295–320.
Groenou, A. B., Bongers, P. F. & Stuyts, A. L. (1968). *Mater. Sci. Eng.* **3**, 317–392.
Groot, F. de, Vankó, G. & Glatzel, P. (2009). *J. Phys. Condens. Matter*, **21**, 104207.
Hagiwara, K., Kanazawa, M., Horie, K., Kokubun, J. & Ishida, K. (1999). *J. Phys. Soc. Jpn*, **68**, 1592–1597.
Hoyt, J. J., de Fontaine, D. & Warburton, W. K. (1984). *J. Appl. Cryst.* **17**, 344–351.
International Tables for X-ray Crystallography (1974). Vol. IV. Birmingham: Kynoch Press.
Kanazawa, M., Hagiwara, K., Kokubun, J. & Ishida, K. (2002). *J. Phys. Soc. Jpn*, **71**, 1765–1770.
Kaneko, Y., Okube, M. & Sasaki, S. (2010). *AIP Conf. Proc.* **1234**, 883–886.
Kobayashi, K., Kawata, H. & Mori, K. (1998). *J. Synchrotron Rad.* **5**, 972–974.
Maruyama, H., Harada, I., Kobayashi, K. & Yamazaki, H. (1995). *Physica B*, **208**–**209**, 760–762.
Matsumoto, K., Saito, F., Toyoda, T., Ohkubo, K., Yamawaki, K., Mori, T., Hirano, K., Tanaka, M. & Sasaki, S. (2000). *Jpn. J. Appl. Phys.* **39**, 6089–6093.
Nishikawa, S. (1915). *Proc. Math. Phys. Soc. Tokyo*, **8**, 199–209.
Okube, M., Furukawa, Y., Yoshiasa, A., Hashimoto, T., Sugahara, M. & Nakatsuka, A. (2008). *J. Phys. Conf. Ser.* **121**, 092004.
Okube, M., Yoshiasa, A., Ohtaka, O., Fukui, H., Katayama, Y. & Utsumi, W. (2002). *Solid State Commun.* **121**, 235–239.
Okudera, H., Kihara, K. & Matsumoto, T. (1996). *Acta Cryst.* B**52**, 450–457.
Pantelouris, A., Modrow, H., Pantelouris, M., Hormes, J. & Reinen, D. (2004). *Chem. Phys.* **300**, 13–22.
Saito, F., Toyoda, T., Mori, T., Tanaka, M., Hirano, K. & Sasaki, S. (1999). *Physica B*, **270**, 35–44.
Sakurai, T. (1967). *X-ray Crystal Structure Analysis*, pp. 338–339. Tokyo: Syokabo. (In Japanese.)
Sasaki, S. (1987). KEK Internal Report 87–3, pp. 1–175. KEK, Tsukuba-shi, Ibaraki, Japan.
Sasaki, S. (1995). *Rev. Sci. Instrum.* **66**, 1573–1578.
Sasaki, S. (1997). *Acta Cryst.* B**53**, 762–766.
Sasaki, S. & Tsukimura, K. (1987). *J. Phys. Soc. Jpn*, **56**, 437–440.
Subias, G., Cuartero, V., Garcia, J., Blasco, J., Mathon, O. & Pascarelli, S. (2009). *J. Phys. Conf. Ser.* **190**, 012089.
Subias, G., Garcia, J., Proietti, M. G., Blasco, J., Renevier, H., Hodeau, J. L. & Sanchez, M. C. (2004). *Phys. Rev. B*, **70**, 155105.
Tanaka, T., Yamashita, H., Tsuchitani, R., Funabiki, T. & Yoshida, S. (1988). *J. Chem. Soc. Faraday Trans. 1*, **84**, 2987–2999.
Templeton, D. H., Templeton, L. K., Phillips, J. C. & Hodgson, K. O. (1980). *Acta Cryst.* A**36**, 436–442.
Thompson, A. C., Attwood, D. T., Gullikson, E. M., Howells, M. R., Kortright, J. B., Robinson, A. L. & Underwood, J. H. (2001). *X-ray Data Booklet*, pp. 1–8, LBNL/PUB-490, Revision 2. Lawrence Berkeley National Laboratory, Berkeley, CA, USA.
Todo, S., Takeshita, N., Kanehara, T., Mori, T. & Mori, N. (2001). *J. Appl. Phys.* **89**, 7347–7349.
Tokonami, M. (1965). *Acta Cryst.* **19**, 486.
Toyoda, T., Sasaki, S. & Tanaka, M. (1997). *Jpn. J. Appl. Phys.* **36**, 2247–2252.
Toyoda, T., Sasaki, S. & Tanaka, M. (1999). *Am. Mineral.* **84**, 294–298.
Tullius, T. D., Gillum, W. O., Carlson, R. M. K. & Hodgson, K. O. (1980). *J. Am. Chem. Soc.* **102**, 5670–5676.
Uhl, M. & Siberchicot, B. (1995). *J. Phys. Condens. Matter*, **7**, 4227–4237.
Verwey, E. J. W. & de Boer, J. H. (1936). *Rec. Trav. Chim.* **55**, 531–540.
Verwey, E. J. W., Haayman, P. W. & Romeijn, F. C. (1947). *J. Chem. Phys.* **15**, 181–187.
Westre, T. E., Kennepohl, P., DeWitt, J. G., Hedman, B., Hodgson, K. O. & Solomon, E. I. (1997). *J. Am. Chem. Soc.* **119**, 6297–6314.
Wu, Z. Y., Xian, D. C., Hu, T. D., Xie, Y. N., Tao, Y., Natoli, C. R., Paris, E. & Marcelli, A. (2004). *Phys. Rev. B*, **70**, 033104.
Yamamoto, T. (2008). *X-ray Spectrom.* **37**, 572–584.
Yanase, A. & Siratori, K. (1984). *J. Phys. Soc. Jpn*, **53**, 312–317.
Zhang, Z. & Satpathy, S. (1991). *Phys. Rev. B*, **44**, 13319–13331.